Radiative Transfer Model for Microwave Bistatic Scattering From Forest Canopies

Pan Liang, *Student Member, IEEE*, Leland E. Pierce, *Senior Member, IEEE*, and
Mahta Moghaddam, *Senior Member, IEEE*

Abstract—A bistatic forest scattering model is developed to simulate scattering coefficients from forest canopies. The model is based on the Michigan Microwave Canopy Scattering (MIMICS) model (hence called Bi-MIMICS) and uses radiative transfer theory, where the first-order fully polarimetric transformation matrix is used. Bistatic radar systems offer advantages over monostatic radar systems because of the additional information provided by the diversity of the geometry. By simulating the forest canopy scattering from multiple viewpoints, we can better understand how the forest scatterers' shape, orientation, density, and permittivity affect the canopy scattering. Bi-MIMICS is parametrized using selected forest stands with different canopy compositions and structure. The simulation results show that bistatic scattering is more sensitive to forest biomass changes than backscattering. Analyzing scattering contributions from different parts of the canopy gives us a better understanding of the microwave's interaction with the tree components. The ground effects can also be studied. Knowledge of the canopy's bistatic scattering behavior combined with additional synthetic aperture radar measurements can be used to improve forest parameter retrievals. The simulation results of the model provide the required information for the design of future bistatic radar systems for forest sensing applications.

Index Terms—Bistatic scattering, forest scattering, radiative transfer, synthetic aperture radar (SAR).

I. INTRODUCTION

BISTATIC radar systems have received increasing attention over the last decade in part due to the advances in communication and processing technologies. Studies and experiments have been reported for system development and algorithms [1], [2]. Bistatic radar measurements have been taken in the laboratory either using radars on two separate platforms or using a monostatic radar with a reflective plane setup [3]–[6]. Some systems have also explored the usage of existing satellite or communication channels as the transmission signals [7], [8].

Bistatic/multistatic radar systems offer advantages over monostatic radar systems in the areas of target detection and identification due to the additional information provided by the bistatic geometry. Targets designed to minimize backscattering radar cross section (RCS) or scattering coefficient (σ_0) may demonstrate a large bistatic RCS, which improves the counterstealth ability of radar systems. If using passive receivers, the receivers are undetectable, which is important for military applications.

Many microwave scattering models have been developed [9]–[15] to better understand the interaction of microwave signals with forests and other vegetated targets, and thereby to assist in forest parameter retrieval from synthetic aperture radar (SAR) measurements. These models, either based on the distorted Born approximation (DBA) [13], [16], [17] or radiative transfer (RT) theory [10], [12], [15], treat forest canopies as infinite horizontal layers over a ground surface. A discrete approach is appropriate with respect to the canopy component size, density, and microwave frequency. The canopy is then characterized as a discrete random medium consisting of single microwave scatterers that represent tree components (i.e., trunks, branches, and foliage). Typically, a crown–trunk layer model is used whereby the upper crown layer contains the branches and foliage (leaves or needles), while the lower layer contains the trunks. The ground is modeled as a rough dielectric surface. These models have been modified and enhanced for various applications and vegetation types to simulate the backscattering RCS.

The existing models, however, have been developed for monostatic (backscattering) radar systems and therefore are insufficient for studying the bistatic RCS of forest canopies. To explore the advantages of bistatic radars, our research has focused on the development of a bistatic model, herein referred to as the bistatic Michigan Microwave Canopy Scattering model (Bi-MIMICS). As the name suggests, the model is based on the original backscattering MIMICS [10]. As with its predecessor and other models, the RT-theory-based canopy scattering model utilizes the discrete scatterer approach and an iterative algorithm to solve the RT equations.

The development of Bi-MIMICS is motivated by the need to design new bistatic systems. The bistatic response of forests can be used in vegetation classification and parameter estimation. By applying the bistatic model to eight hypothetical deciduous (Aspen) and coniferous (White Spruce) forest canopies at various observation angles, the simulation results enhance the understanding of how a forest's structure, scatterer orientation, density, and diversity affect the scattering measurements. As a result, better understanding of the microwave scattering mechanisms of tree components are obtained, which aid studies such as communication channel sensitivity in forested areas as well as detection of targets under the trees. The model can also be used to study the effects of the underlying ground on total scattering. The simulation results of the model offer the needed information for the design of future bistatic radar systems for forest sensing applications. In this research, we apply Bi-MIMICS to a number of canopies at different angles, frequencies, and polarizations. The simulated bistatic RCS is examined for the canopy's scattering signature and the dependency on angle, frequency, and polarization.

This paper is organized as follows. Section II provides a brief background to and overview of the backscattering version of MIMICS on which the bistatic model is based. The development of Bi-MIMICS is then presented in Section III. Section IV describes canopy parameters and bistatic geometry setup. The application of Bi-MIMICS to selected canopies and the simulation results are discussed in Section V, and Section VI concludes the study.

II. BACKGROUND

An overview of the main elements of MIMICS is provided here in order to provide context for the changes we have made and describe in the next section. MIMICS [10] was developed to model microwave backscattering from vegetation canopies. The model was based on radiative transfer theory. The vertical canopy structure was modeled as two cascading independent horizontal vegetation layers over a dielectric ground surface. The top crown layer was composed of an ensemble of leaves, needles, and branches, while tree trunks made up the lower trunk layer. All the tree components were treated like single microwave scatterers: leaves were modeled as flat circular disks; branches, and needles were modeled as dielectric cylinders or prolate spheroids; and trunks were again modeled as large cylinders. The underlying ground was modeled as a rough dielectric surface that was specified by a root mean square (RMS) height and a correlation length. Trees were assumed uniformly distributed over the ground, and the scattering components within each layer were characterized by the statistics of their sizes, positions, orientations, and densities.

The RT theory utilizes two processes—extinction and emission to describe the change of propagating microwave intensity in a given direction caused by the medium [18]. Extinction refers to the decrease in magnitude of the wave intensity along the propagation path either by absorption or scattering into other directions. Emission accounts for the increase in magnitude of the wave intensity along the propagation path due to both emission and scattering into the propagating directions from other directions [18]. The self-thermal emission from the canopy is negligible compared to other sources at the frequencies used in active radar remote sensing. For a single particle, a modified Mueller matrix is often used to transform the incident intensity to the scattered intensity by defining both as modified Stokes vectors. For a medium containing random particles, the waves scattered from these particles are random in phase under the RT theory assumption, and therefore, the total scattered wave energy can be calculated by incoherent summation over all the particles. Thus, the extinction and emission processes within each layer can be represented mathematically by both the average extinction and source matrices of that layer.

The incident energy is reflected and scattered by the ground surface, which is denoted by scattering and reflectivity matrices. The diffuse boundary condition assumes that the wave intensities across the interfaces are continuous. MIMICS solves the RT equations to find the transformation matrix relating the incident intensity and the scattering intensity. Seven terms [10], which represent the seven scattering mechanisms (Fig. 1) for wave energy propagating through the canopy down to the ground surface, reflected and backscattered from the ground surface, and
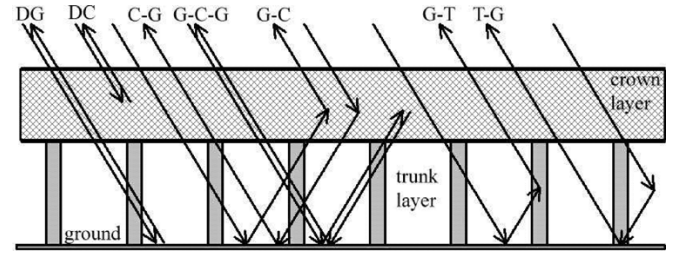

Fig. 1. Seven backscattering terms in the first-order MIMICS solution based on RT theory, including DG (direct ground), DC (direct crown backscattering), C-G (crown scattering and ground reflection), G-C (ground reflection and crown scattering), G-C-G (ground reflection and crown scattering and ground reflection), (T-G) trunk scattering and ground reflection, and (G-T) ground reflection and trunk scattering.

propagating back through the canopy, are included in the first-order MIMICS solution.

There are four backscatter sources in the crown layer: 1) direct backscattering from the crown layer; 2) crown specular scattering followed by ground reflection; 3) ground reflection followed by crown specular scattering; and 4) double bounce by ground reflection and crown backscattering and ground reflection. In the trunk layer, for the nearly vertically oriented large cylindrical trunks, backscattering vanishes. Direct backscattering from the trunk layer and double-bounce terms between the trunk and crown layers become insignificant; hence only two mechanisms are included. They are: 1) trunk specular scattering followed by ground reflection and 2) ground reflection followed by trunk specular scattering. One additional item included is the backscattering from the ground surface.

MIMICS is valid in the range of 0.5–10 GHz at incidence angles greater than $10°$. The model has been validated and widely applied to estimate the microwave backscattering coefficients of various canopies in many studies. In a scatterometer experiment presented in [19] and [20], MIMICS simulated the L-band backscattering coefficient from a walnut orchard and was validated by measurements, although the simulation results showed some discrepancies at X-band. The problem was attributed to higher order scattering contributions, and the discontinuity of the canopy. MIMICS has also been applied to the Alaskan Boreal Forest [21] to study the effects of thawing and freezing soil on the radar backscatter.

III. BISTATIC MIMICS MODEL DEVELOPMENT

A. Radiative Transfer Equations and Solution

The original version of MIMICS [10] was built using bistatic scattering models of each canopy constituent. These models were combined into a backscatter-only radiative transfer canopy model. More factors need to be considered for the bistatic canopy scattering model. Consider the geometry of Fig. 2; the downward incident intensity $\mathbf{I}_0$ impinges on the top surface of the canopy at an angle (θ_0, ϕ_0). The upward scattering intensity $\mathbf{I}_s$ is in the direction (θ, ϕ). For simplicity, the incidence azimuth angle ϕ_0 is set to be zero. Three angle parameters defining the incidence and scattering angle are shown in Fig. 2. Under this definition, the set $\{\theta = \theta_0, \phi = 180°\}$ indicates backscattering; $\{\theta = \theta_0, \phi = 0\}$ stands for specular scattering; and $\{\theta = \pi - \theta_0, \phi = 0\}$ denotes forward scattering.
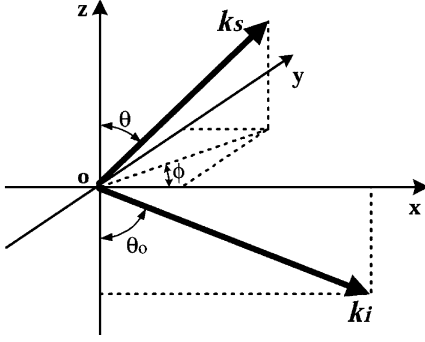
Fig. 2.   Bistatic simulation angles. Incident direction (downward) is in the x-z plane and defined by incidence angle θ_0 and $\phi_0 = 0$. Scattering direction (upward) is defined by θ and ϕ.
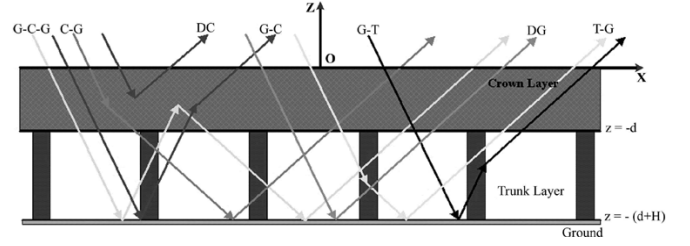

Fig. 3.   Scattering mechanisms in the first-order Bi-MIMICS solution based on RT theory, including G-C-G (ground reflection and crown scattering and ground reflection), C-G (crown scattering and ground reflection), DC (direct crown backscattering), G-C (ground reflection and crown scattering), G-T (ground reflection and trunk scattering), DG (direct ground), and T-G (trunk scattering and ground reflection). The specular ground reflection is not shown in the figure. Crown layer depth $= d$,   Trunk layer height $= H$.

The polarization state of the intensity is represented by the modified Stokes vector as follows:

$$\mathbf{I} = \begin{bmatrix} I_v \\ I_h \\ U \\ V \end{bmatrix} \Big/ \eta = \begin{bmatrix} |E_v|^2 \\ |E_h|^2 \\ 2\Re(E_v E_h^*) \\ 2\Im(E_v E_h^*) \end{bmatrix} \Big/ \eta \qquad (1)$$

where E_v and E_h are the vertical and horizontal polarized parts of the electrical field vector, respectively. The quantity η is the intrinsic impedance. The intensity scattered by a single particle can be related to the incident intensity by the modified Mueller matrix $\mathcal{L}_m$ [22]

$$\mathbf{I}_s(\theta, \phi) = \frac{1}{r^2} \mathcal{L}_m(\theta, \phi; \theta_0, \phi_0; \theta_k, \phi_k) \mathbf{I}_0(\theta_0, \phi_0) \qquad (2)$$

where (θ_k, ϕ_k) is the orientation of the particle and r is the distance of the scattered intensity from the particle. The modified Mueller matrix $\mathcal{L}_m$ is defined by the electrical field scattering matrix S of the particle as in (3), shown at the bottom of the page.

In Bi-MIMICS, the first-order bistatic transformation matrix $\mathcal{T}$ transforms the incident intensity into the scattering intensity by

$$\mathbf{I}_s(\mu, \phi) = \mathcal{T}(\mu, \phi) \mathbf{I}_0(\mu_0, \phi_0) \qquad (4)$$

where $(\mu_0 = \cos\theta_0, \phi_0)$ defines the incidence direction and $(\mu = \cos\theta, \phi)$ is the scattered direction. The seven scattering

mechanisms described in backscattering MIMICS still exist, but they are measured in bistatic directions as shown in Fig. 3. In addition, the ground reflection in the specular direction needs to be included. Fig. 3 also shows the canopy structure above the ground. The depths of the crown and trunk layer are denoted by d and H, respectively.

The transformation matrix $\mathcal{T}$ is given in terms of the extinction and phase matrices. The extinction and phase matrices are calculated by the average modified Mueller matrices over the canopy composite scatterers. For a medium containing one type of scatterer whose size s_k and orientation (θ_k, ϕ_k) can be described by a certain distribution, $f(s_k; \theta_k, \phi_k)$, its phase matrix is given by

$$\mathcal{P}(\theta, \phi; \theta_0, \phi_0) = N_k \iiint f(s_k; \theta_k, \phi_k)$$
$$\times \mathcal{L}_m(\theta, \phi; \theta_0, \phi_0; \theta_k, \phi_k) \, ds_k \, d\theta_k \, d\phi_k \qquad (5)$$

where N_k is the scatterer number density. If the medium contains more type of scatterers, the total phase matrix of the medium is the summation of phase matrices over all types. The extinction matrix of a medium containing random scatterers [22], [23] is given by (6) and (7), where K is the total type of scatterers in the medium, N_k is the number density of type k, $\langle S_{pqk}(\theta, \phi; \theta_0, \phi_0; \theta_k, \phi_k) \rangle_k$ is the average scattering amplitude coefficient of type k scatterers at pq polarization, and k_0 is the free-space wavenumber, as in (6) and (7), shown at the bottom of the page.

$$\mathcal{L}_m = \begin{bmatrix} |S_{\mathrm{vv}}|^2 & |S_{\mathrm{vh}}|^2 & \Re(S_{\mathrm{vh}}^* S_{\mathrm{vv}}) & -\Im(S_{\mathrm{vh}}^* S_{\mathrm{vv}}) \\ |S_{\mathrm{hv}}|^2 & |S_{\mathrm{hh}}|^2 & \Re(S_{\mathrm{hh}}^* S_{\mathrm{hv}}) & -\Im(S_{\mathrm{hv}} S_{\mathrm{hh}}^*) \\ 2\Re(S_{\mathrm{vv}} S_{\mathrm{hv}}^*) & 2\Re(S_{\mathrm{vh}} S_{\mathrm{hh}}^*) & \Re(S_{\mathrm{vv}} S_{\mathrm{hh}}^* + S_{\mathrm{vh}} S_{\mathrm{hv}}^*) & -\Im(S_{\mathrm{vv}} S_{\mathrm{hh}}^* - S_{\mathrm{vh}} S_{\mathrm{hv}}^*) \\ 2\Im(S_{\mathrm{vv}} S_{\mathrm{hv}}^*) & 2\Im(S_{\mathrm{vh}} S_{\mathrm{hh}}^*) & \Im(S_{\mathrm{vv}} S_{\mathrm{hh}}^* + S_{\mathrm{vh}} S_{\mathrm{hv}}^*) & \Re(S_{\mathrm{vv}} S_{\mathrm{hh}}^* - S_{\mathrm{vh}} S_{\mathrm{hv}}^*) \end{bmatrix} \Big/ \eta \qquad (3)$$

$$\boldsymbol{\kappa} = \begin{bmatrix} -2\Re(M_{\mathrm{vv}}) & 0 & -\Re(M_{\mathrm{vh}}) & -\Im(M_{\mathrm{vh}}) \\ 0 & -2\Re(M_{\mathrm{hh}}) & -\Re(M_{\mathrm{hv}}) & \Im(M_{\mathrm{hv}}) \\ -2\Re(M_{\mathrm{hv}}) & -2\Re(M_{\mathrm{vh}}) & -\Re(M_{\mathrm{vv}} + M_{\mathrm{hh}}) & \Im(M_{\mathrm{vv}} - M_{\mathrm{hh}}) \\ 2\Im(M_{\mathrm{hv}}) & -2\Im(M_{\mathrm{vh}}) & -\Im(M_{\mathrm{vv}} - M_{\mathrm{hh}}) & -\Re(M_{\mathrm{vv}} + M_{\mathrm{hh}}) \end{bmatrix} \qquad (6)$$

$$M_{pq} = \sum_{k=1}^{K} \frac{i 2\pi N_k}{k_0} \langle S_{pqk}(\theta, \phi; \theta_0, \phi_0; \theta_k, \phi_k) \rangle_k; \quad p, q = v, h \qquad (7)$$

The transformation matrix $\mathcal{T}$ is given by

$$
\begin{aligned}
\mathcal{T}(\mu,\phi) =\ & e^{-\boldsymbol{\kappa}_c^+ d/\mu} e^{-\boldsymbol{\kappa}_t^+ H/\mu} \mathcal{R}(\mu) e^{-\boldsymbol{\kappa}_t^- H/\mu} \\
& \times e^{-\boldsymbol{\kappa}_c^- d/\mu} \delta(\mu - \mu_0)\delta(\phi - \phi_0) \\
& + \frac{1}{\mu} e^{-\boldsymbol{\kappa}_c^+ d/\mu} e^{-\boldsymbol{\kappa}_t^+ H/\mu} \mathcal{R}(\mu) e^{-\boldsymbol{\kappa}_t^- H/\mu} \\
& \times \mathcal{A}_{\mathrm{cgc}}(-\mu,\phi,\mu_0,\phi_0) e^{-\boldsymbol{\kappa}_t^+ H/\mu_0} \mathcal{R}(\mu_0) \\
& \times e^{-\boldsymbol{\kappa}_t^- H/\mu_0} e^{-\boldsymbol{\kappa}_c^- d/\mu_0} \\
& + \frac{1}{\mu} e^{-\boldsymbol{\kappa}_c^+ d/\mu} e^{-\boldsymbol{\kappa}_t^+ H/\mu} \mathcal{R}(\mu) \\
& \times e^{-\boldsymbol{\kappa}_t^- H/\mu} \mathcal{A}_{\mathrm{cg}}(-\mu,\phi,-\mu_0,\phi_0) \\
& + \frac{1}{\mu} \mathcal{A}_{\mathrm{gc}}(\mu,\phi,\mu_0,\phi_0) e^{-\boldsymbol{\kappa}_t^+ H/\mu_0} \mathcal{R}(\mu_0) \\
& \times e^{-\boldsymbol{\kappa}_t^- H/\mu_0} e^{-\boldsymbol{\kappa}_c^- d/\mu_0} \\
& + \frac{1}{\mu} \mathcal{A}_{\mathrm{dc}}(\mu,\phi,-\mu_0,\phi_0) \\
& + \frac{1}{\mu} e^{-\boldsymbol{\kappa}_c^+ d/\mu} e^{-\boldsymbol{\kappa}_t^+ H/\mu} \mathcal{R}(\mu) \\
& \times \mathcal{A}_{\mathrm{tg}}(-\mu,\phi,-\mu_0,\phi_0) e^{-\boldsymbol{\kappa}_c^- d/\mu_0} \delta(\mu - \mu_0) \\
& + \frac{1}{\mu} e^{-\boldsymbol{\kappa}_c^+ d/\mu} \mathcal{A}_{gt}(\mu,\phi,\mu_0,\phi_0) \mathcal{R}(\mu_0) \\
& \times e^{-\boldsymbol{\kappa}_t^- H/\mu_0} e^{-\boldsymbol{\kappa}_c^- d/\mu_0} \delta(\mu - \mu_0) \\
& + e^{-\boldsymbol{\kappa}_c^+ d/\mu} e^{-\boldsymbol{\kappa}_t^+ H/\mu} \mathcal{G}(\mu,\phi,-\mu_0,\phi_0) \\
& \times e^{-\boldsymbol{\kappa}_t^- H/\mu_0} e^{-\boldsymbol{\kappa}_c^- d/\mu_0}
\end{aligned} \tag{8}
$$

We denote the upward extinction matrix by $\boldsymbol{\kappa}^+$ and the downward extinction matrix by $\boldsymbol{\kappa}^-$. The subscripts c and l indicate the crown and trunk layer, respectively. The quantity $\mathcal{R}$ is the reflectivity matrix of the specular ground surface, and $\mathcal{G}$ represents the ground scattering matrix. The $\mathcal{A}$ terms represent the scattering occurring in the crown and trunk layer, which could be obtained by proper phase matrices and extinction matrices [23]. The first term in $\mathcal{T}$ denotes the specular ground reflection, while the next four terms are contributions from the crown layer. Two types of ground–trunk interaction are represented by the sixth and seventh term, and the last term is the direct bistatic scattering from the rough ground surface.

The term $\mathcal{A}_{\mathrm{gcg}}$ indicates the scattering contribution to the ground–scatterer mechanism. The term $\mathcal{A}_{\mathrm{cg}}$ accounts for the scatterer–ground effect by the crown layer. The term $\mathcal{A}_{\mathrm{gc}}$ is the complement of $\mathcal{A}_{\mathrm{cg}}$ and shows that the incident intensity is first reflected by the ground and then scattered into the direction (μ,ϕ) by the crown layer. The term $\mathcal{A}_{\mathrm{dc}}$ is the direct bistatic scattering by the crown layer. The terms $\mathcal{A}_{\mathrm{tg}}$ and $\mathcal{A}_{gt}$ represent the scattering by the trunk layer and ground interactions, similar to $\mathcal{A}_{\mathrm{cg}}$ and $\mathcal{A}_{\mathrm{gc}}$.

The term $\mathcal{A}_{\mathrm{gcg}}$ integrates the wave intensity that is scattered from the upward direction $(\mu_0,0)$ to the downward direction $(-\mu,\phi)$ through the crown layer, which is also attenuated along the propagation path. Similar approaches are applied to get the other $\mathcal{A}$ integrals as shown in (9), where $\mathcal{P}_c$ and $\mathcal{P}_t$ are the average phase matrices for the crown and trunk layer, respectively, in which the angle argument of $(\mu_s,\phi_s,\mu_i,\phi_i)$ indicates that

the wave intensity is scattered from the (μ_i,ϕ_i) direction to the (μ_s,ϕ_s) direction

$$
\begin{aligned}
\mathcal{A}_{\mathrm{cgc}}(-\mu,\phi,\mu_0,\phi_0) &= \int_{-d}^{0} e^{-\boldsymbol{\kappa}_c^-(d+z')/\mu} \\
& \cdot \mathcal{P}_c(-\mu,\phi,\mu_0,\phi_0) e^{-\boldsymbol{\kappa}_c^+(z'+d)/\mu_0}\, \mathrm{d}z' \\
\mathcal{A}_{\mathrm{cg}}(-\mu,\phi,-\mu_0,\phi_0) &= \int_{-d}^{0} e^{-\boldsymbol{\kappa}_c^-(d+z')/\mu} \\
& \cdot \mathcal{P}_c(-\mu,\phi,-\mu_0,\phi_0) e^{mmb\boldsymbol{\kappa}_c^- z'/\mu_0}\, \mathrm{d}z' \\
\mathcal{A}_{\mathrm{gc}}(\mu,\phi,\mu_0,\phi_0) &= \int_{-d}^{0} e^{\boldsymbol{\kappa}_c^+ z'/\mu} \\
& \cdot \mathcal{P}_c(\mu,\phi,\mu_0,\phi_0) e^{-\boldsymbol{\kappa}_c^+(z'+d)/\mu_0}\, \mathrm{d}z' \\
\mathcal{A}_{\mathrm{dc}}(\mu,\phi,-\mu_0,\phi_0) &= \int_{-d}^{0} e^{\boldsymbol{\kappa}_c^+ z'/\mu} \\
& \cdot \mathcal{P}_c(\mu,\phi,-\mu_0,\phi_0) e^{\boldsymbol{\kappa}_c^- z'/\mu_0}\, \mathrm{d}z' \\
\mathcal{A}_{\mathrm{tg}}(-\mu,\phi,-\mu_0,\phi_0) &= \int_{-(d+H)}^{-d} e^{-\boldsymbol{\kappa}_t^-(H+z')/\mu} \\
& \cdot \mathcal{P}_t(-\mu,\phi,-\mu_0,\phi_0) e^{\boldsymbol{\kappa}_t^-(z'+d)/\mu_0}\, \mathrm{d}z' \\
\mathcal{A}_{gt}(\mu,\phi,\mu_0,\phi_0) &= \int_{-(d+H)}^{-d} e^{\boldsymbol{\kappa}_t^+(d+z')/\mu} \\
& \cdot \mathcal{P}_t(\mu,\phi,\mu_0,\phi_0) e^{-\boldsymbol{\kappa}_t^+(z'+d+H)/\mu_0}\, \mathrm{d}z'.
\end{aligned} \tag{9}
$$

The reflectivity matrix of the specular ground surface is given by

$$
\mathcal{R}(\mu) = \begin{bmatrix} |r_v|^2 & 0 & 0 & 0 \\ 0 & |r_h|^2 & 0 & 0 \\ 0 & 0 & \mathrm{Re}(r_v r_h^*) & -\mathrm{Im}(r_v r_h^*) \\ 0 & 0 & \mathrm{Im}(r_v r_h^*) & \mathrm{Re}(r_v r_h^*) \end{bmatrix} \tag{10}
$$

where r_v and r_h are the specular reflection coefficients at vertical and horizontal polarizations, respectively. The ground scattering matrix $\mathcal{G}$ is calculated from rough surface scattering models.

B. Model Implementation

For every type of canopy component, several analytical and empirical models are provided for different regions of validity with respect to their shapes and sizes [23]. Trunks and branches are modeled as homogeneous dielectric cylinders with mean length l and mean diameter d. Prolate Rayleigh spheroids are used to model small cylinders ($l \ll \lambda$), which includes small branches and needles. For many types of intermediate size branches, a long ($l \gg \lambda$) and thin ($d \ll \lambda$) cylinder model is used. As for large branches and trunks, an appropriate approximation is derived from the infinitely long large cylinder scattering model. Leaves are modeled as dielectric circular disks with a thickness and diameter. Two scattering models are used for leaves—an oblate Rayleigh spheroid or a physical optics model, depending on the disk diameter. The dielectric constants of various canopy constituents are determined from their moisture contents through analytical and empirical models [24], [25].
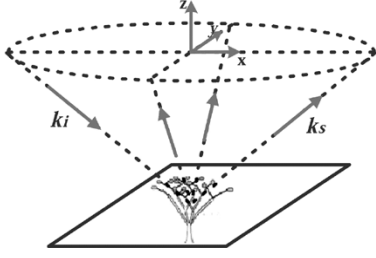
Fig. 4. Specular direction cone surface. Incidence angle θ = scattering angle θ_0, $0 \le \phi \le 360°$ forms a cone surface.

Fig. 5. Branch orientation pdf in the vertical direction of the aspen stand and white spruce stand.

TABLE I
CANOPY PARAMETERS FOR SIMULATIONS

Parameters	Aspen	White Spruce
Trunk Density (number/ha)	1100	2000
Trunk Height (m)	8	16
Trunk Diameter (cm)	24	20.8
Trunk Moisture (gravimetric)	0.5	0.6
Crown Depth (m)	2	11
Leaf Density (number/m^3)	0	85000
Leaf Moisture (gravimetric)	-	0.8
LAI(single sided)	0	11.9
Branch Density (number/m^3)	4.1	3.4
Branch Length (m)	0.75	2.0
Branch Diameter (cm)	0.7	2.0
Branch Moisture (gravimetric)	0.4	0.6
Soil RMS Height (cm)	0.45	0.45
Correlation Length (cm)	18.75	18.75
Soil Moisture (volumetric)	0.15	0.15
Soil % Sand	10	20
Soil % Silt	30	70
Soil % Clay	60	10

TABLE II
RELATIVE PERMITTIVITIES OF CANOPY CONSTITUENTS. CONSTANTS WERE USED IN THE FREQUENCY RANGE WE USED IN THIS PAPER, BECAUSE THESE VALUES WERE SLOWLY VARYING

Stand	Soil	Trunk	Branch	Foliage
Aspen	5.99 -j 0.99	14.49 -j 4.76	10.19 -j 3.36	-
White Spruce	6.27 -j 1.55	16.45 -j 7.31	16.45 -j 7.31	27.00 -j12.43

Three rough surface models, geometrical optics (GO), physical optics (PO), and small perturbation (SP) model, are provided to simulate different roughness scales of the ground. Generally, the GO model is best suited for rough surfaces; the PO model is suitable for surfaces with intermediate scales of roughness; and the SP model is suitable for surfaces with short correlation lengths. The amount of roughness is important at the scale of the wavelength that one is using, and so these models are best chosen by the analyst to provide the best model for the roughness/frequency combination of interest. The bistatic radar RCS measurements taken for surfaces with artificial roughness using a 10-GHz bistatic system [26] were consistent with rough surface models' simulations.
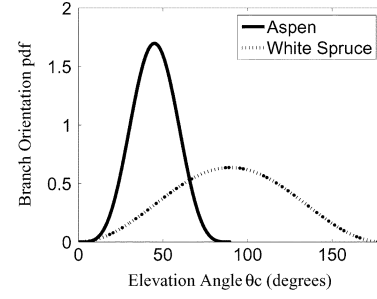
Two angle parameters θ and ϕ are added as compared with backscattering MIMICS. In the calculation of the upward and downward extinction matrices for the crown and trunk layers, both directions are needed instead of one direction as in backscattering MIMICS. Therefore, four types of angle combinations are chosen to calculate the attenuating extinction matrices: two upward directions $(\theta_0, 0)$ and (θ, ϕ) and two downward directions $(\pi - \theta_0, 0)$ and $(\pi - \theta, \phi)$. Similarly, this is also done for the phase matrices. Four angle transformations are necessary to calculate the phase matrices: from $(\theta_0, 0)$ to (θ, ϕ), from $(\theta_0, 0)$ to $(\pi - \theta, \phi)$, from $(\pi - \theta_0, 0)$ to (θ, ϕ), and from $(\pi - \theta_0, 0)$ to $(\pi - \theta, \phi)$. When we calculate the $\mathcal{A}$ integrals, unlike the backscattering case, the extinction matrices $\boldsymbol{\kappa}$ before scattering are not in the parallel direction to those after scattering; therefore, the azimuthal symmetry of canopy [i.e., $\boldsymbol{\kappa}(\mu_0, 0) = \boldsymbol{\kappa}(\mu_0, \pi)$] is only valid for the special backscattering case, and for the general cases both the angles θ_0 and θ need to be calculated.

The downward microwave intensities are reflected by the ground surface at two angles related to the location from which the scattering happens: if the wave is first scattered by the crown or trunk layer from $(-\mu_0, 0)$ direction to $(-\mu, \phi)$ direction before it penetrates to the ground, the ground reflection angle is then θ, and the ground reflectivity matrix is $\mathcal{R}(\mu)$. However, if the penetrating wave is first reflected by the ground and then scattered by the vegetation layers, the ground reflection angle is then θ_0 and the ground reflectivity matrix is $\mathcal{R}(\mu_0)$. For the crown double-bounce scattering mechanism, θ_0 is the first ground reflection angle, and θ is for the second ground reflection. Therefore, two ground reflectivity matrices $\mathcal{R}(\mu)$ and $\mathcal{R}(\mu_0)$ are needed as compared to MIMICS, which only calculates $\mathcal{R}(\mu_0)$.
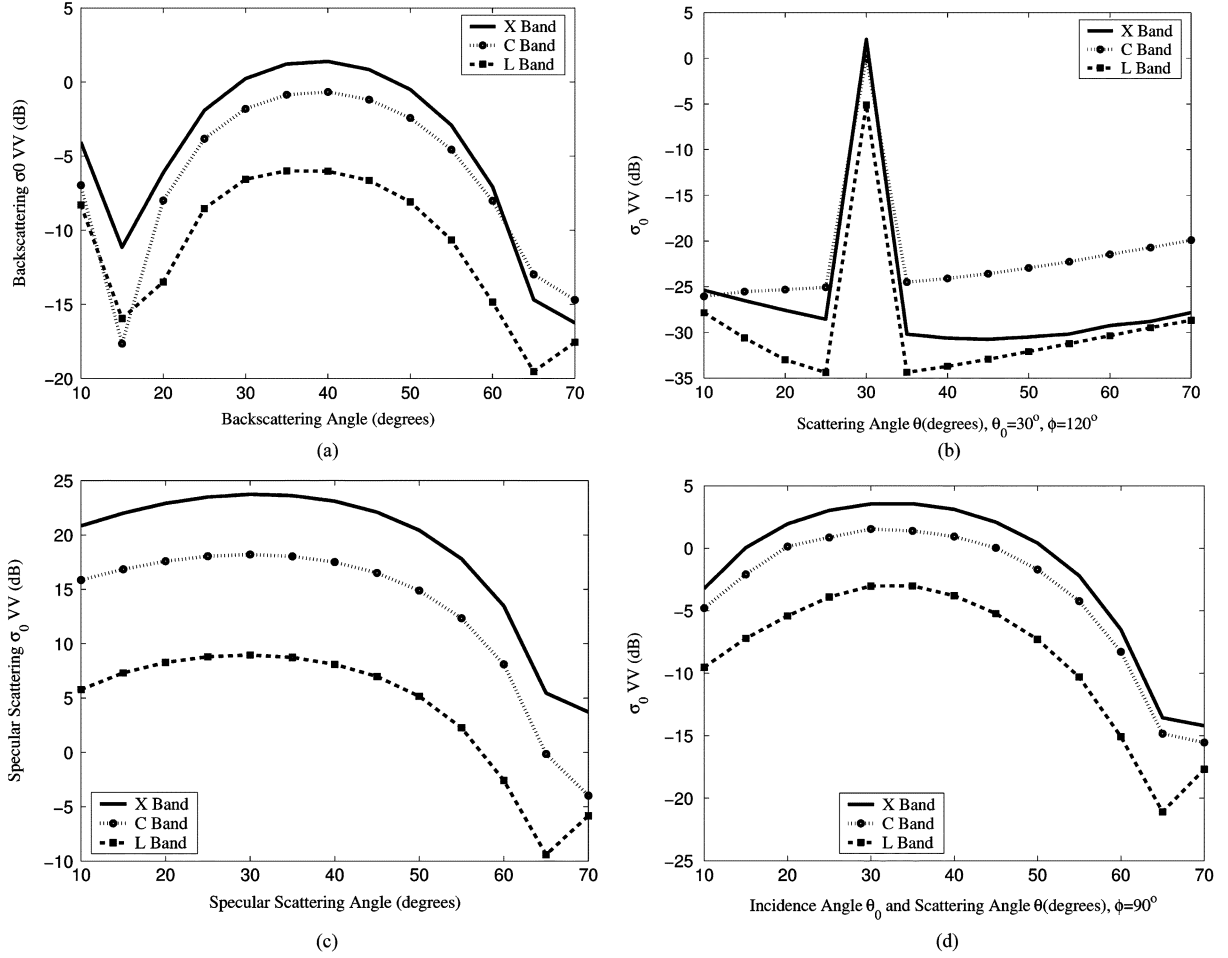
Fig. 6. VV-polarized canopy scattering cross section versus scattering angle from aspen for L-, C-, and X-bands at (a) backscattering plane, (b) $\theta_0 = 30°$ and $\phi = 120°$, (c) specular plane, and (d) perpendicular plane $(\theta = \theta_0, \phi = 90°)$. The spike in (b) is due to specular scattering and is only wide in these plots due to the fact that we are sampling every 5° and connecting consecutive points with lines. (a) Backscattering. (b) Bistatic scattering. (c) Specular scattering. (d) Perpendicular plane.

Bi-MIMICS calculates the average bistatic extinction matrices and phase matrices of the combination of scatterers in the crown and trunk layer, reflectivity matrices and scattering matrices of the ground at certain angles, and then places them together through proper attenuation and scattering to get the total canopy transformation matrix.

IV. MODEL SIMULATION PARAMETERS SETUP

A. Sensor Parameters

We simulate the fully polarized microwave scattering [horizontal (HH), horizontal–vertical (HV), vertical–horizontal (VH), vertical (VV)] for the canopies at L-, C-, and X-bands. The frequencies are 1.6, 4.75, and 10 GHz, respectively. Various bistatic observation angle combinations are simulated. Backscattering plane, specular scattering plane, and specular direction cone surface are paid special attention because the trunk scattering is the strongest on these surfaces. When the observation direction is outside of these surfaces, the trunk layer functions only as an attenuating layer since the trunk

scattering is very weak. The specular direction cone surface is shown in Fig. 4.

B. Canopy Parameters

Two types of canopies are chosen for the bistatic scattering simulation. One is a deciduous tree stand of defoliated aspen. The other is a conifer tree stand of white spruce. The relevant canopy parameters are listed in Table I. The canopy data are collected from [10]. A PO model is used for the ground surface.

The trunks are vertical, and the orientations of the crown components are assumed to be uniformly distributed in the horizontal direction. For the aspen stand, the branch angle probability density function (pdf) in the vertical direction is chosen as $p(\theta_c) = (16/3\pi) \sin^4(2\theta_c), 0 \leq \theta_c \leq 90°$. For the white spruce stand, the branch orientation pdf in the vertical direction is chosen as $p(\theta_c) = (2/\pi) \sin^2(\theta_c), 0 \leq \theta_c \leq 180°$. Fig. 5 shows the pdfs of the branch orientation of the two stands.

At an environmental temperature of 20 °C, the permittivities for the ground and canopy components are calculated and listed in Table II.
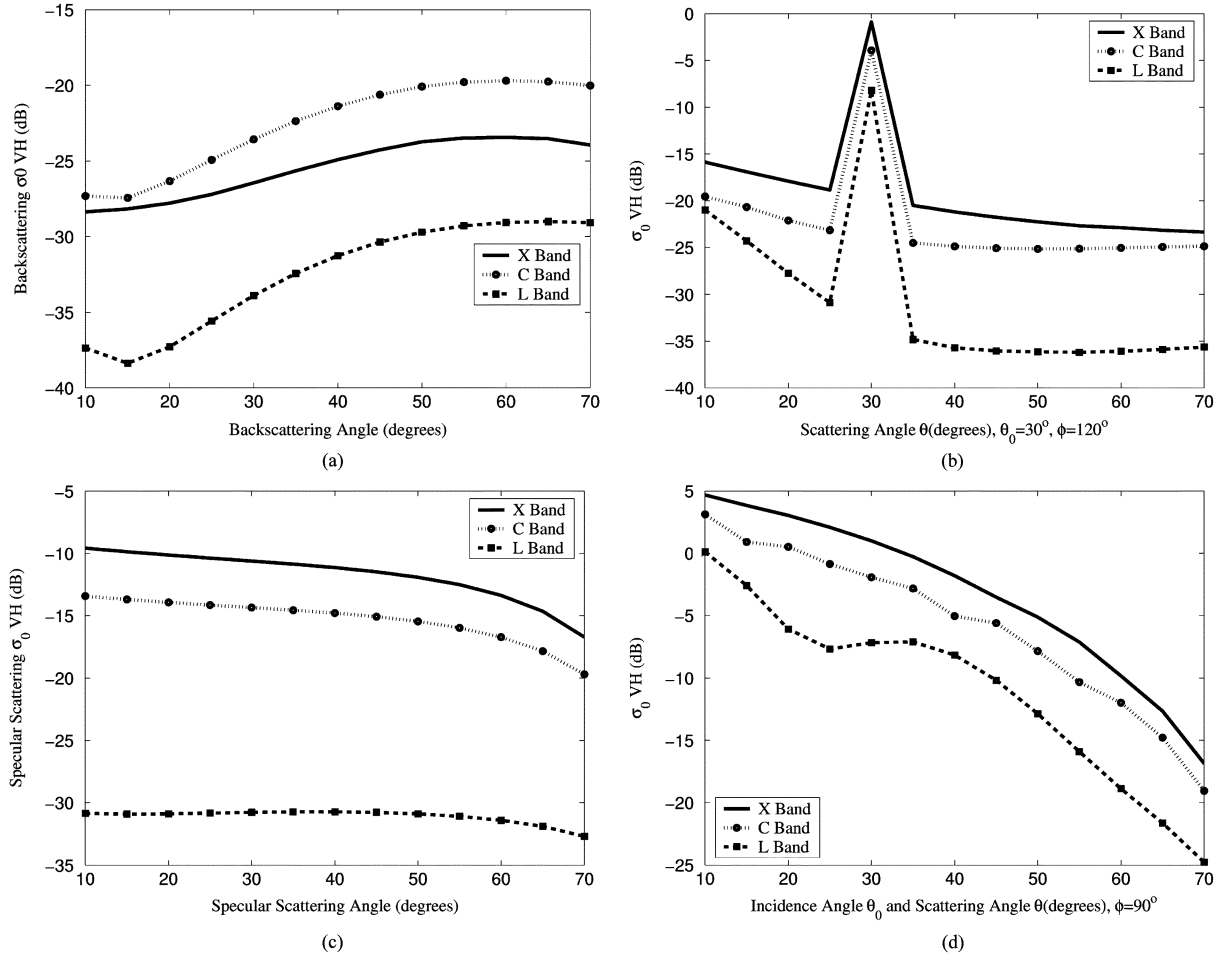
Fig. 7.   VH-polarized canopy scattering cross section versus scattering angle from aspen for L-, C-, and X-bands at (a) backscattering plane and (b) $\theta_0 = 30°$ and $\phi = 120°$. (c) Specular plane. (d) Perpendicular plane ($\theta = \theta_0, \phi = 90°$). The spike in (b) is due to specular scattering and is only wide in these plots due to the fact that we are sampling every $5°$ and connecting consecutive points with lines. (a) Backscattering. (b) Bistatic scattering. (c) Specular scattering. (d) Perpendicular plane.

V. SIMULATION RESULTS AND ANALYSIS

A. Comparison With Backscattering MIMICS

For each canopy and incidence angle, we compare the backscattering σ_0 simulated by Bi-MIMICS and standard MIMICS. Not surprisingly, the two models provide the same results. Although we do not have measured bistatic data and hence cannot validate the Bi-MIMICS simulated bistatic σ_0 with existing radar measurements, backscattering MIMICS has been verified on actual forest inventory data and SAR data over the years [15], [19]–[21]. The consistency between two models indicates that Bi-MIMICS is an effective canopy scattering model for the special backscattering case. We await future measurements for proper validation of this model.

B. Bistatic Scattering Simulation for Aspen

Based on the model input parameters, simulation of SAR scattering at all frequencies and polarizations is undertaken using Bi-MIMICS for multiple observation angles. We present the VV-polarized total scattering from the aspen stand in Fig. 6. Figs. 6(a) and (c) are for the backscattering and specular cases respectively, when the elevation angle θ is in the range of $10°$

to $70°$. In Fig. 6(b), the angles $\theta_0 = 30°$, $\phi = 120°$ are fixed while θ changes from $10°$ to $70°$. Fig. 6(d) plots the observation made in the plane perpendicular to ($\theta = \theta_0, \phi = 90°$) the incident direction. The figures show that the overall scattering in the specular direction is the strongest, as expected. Fig. 6(b) indicates that this aspen stand is a trunk-dominated canopy since we observe a scattering peak at $\theta = \theta_0 = 30°$, which includes the trunk's contribution. At other angles of θ, the much lower level of the scattering coefficient is from the crown layer and ground. Fig. 6(a), (c), and (d) also indicate that more canopy VV-polarized scattering occurs at higher frequencies because of much stronger scattering from the trunk–ground and crown–ground interactions. However, the strongest direct crown scattering and double-bounce scattering between the crown and ground occur at C-band due to lower volume scattering at L-band and more crown attenuation at X-band, which is shown by Fig. 6(b). The figure shows that C-band has the highest bistatic scattering coefficient σ_0 when trunk scattering is not present.

As for the cross polarization, VH-polarized σ_0 demonstrates a different canopy response at the observation angles as shown
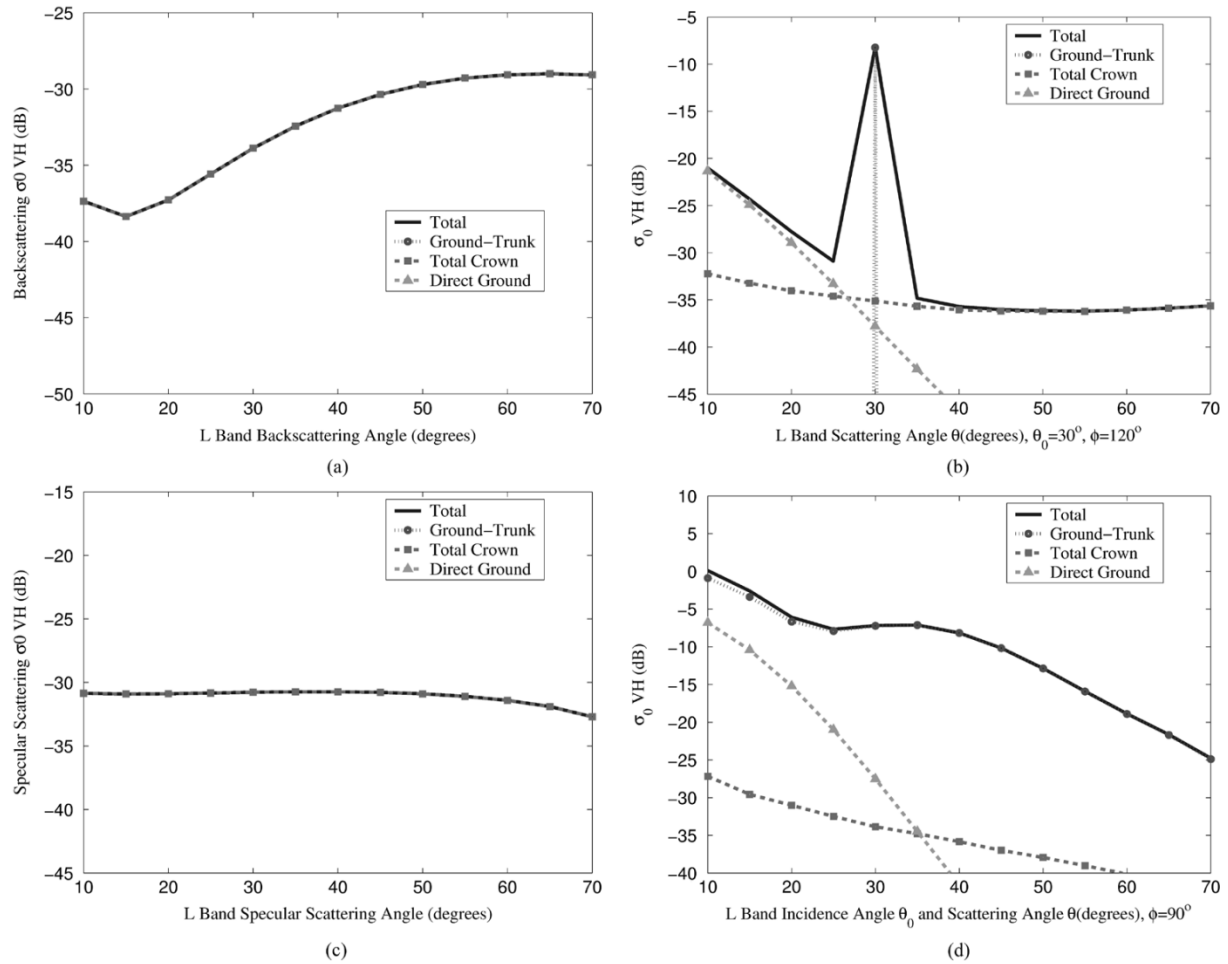
Fig. 8. L-band VH-polarized canopy scattering component contributions versus scattering angle from aspen at (a) backscattering plane and (b) $\theta_0 = 30°$ and $\phi = 120°$. (c) Specular plane. (d) Perpendicular plane ($\theta = \theta_0, \phi = 90°$). The spike in (b) is due to specular scattering and is only wide in these plots due to the fact that we are sampling every $5°$ and connecting consecutive points with lines. (a) Backscattering. (b) Bistatic scattering. (c) Specular scattering. (d) Perpendicular plane.

in Fig. 7. The component contributions to the total scattering at L-band are shown in Fig. 8. The C-band VH-polarized backscattering RCS exceeds the X-band result [Fig. 7(a)] in contrast to the other three configurations, in which the X-band gives the strongest scattering coefficient. Figs. 7 and 8 also demonstrate that crown–ground interactions are the major part of VH-backscattering RCS, and C-band has the largest value for moderate scattering and moderate attenuation compared to the other two bands. The trunk–ground interactions provide little VH polarization scattering contribution in the backscattering and specular direction as in Fig. 8(a) and (c); the trunk and ground scattering are too low to be shown in the figures. In contrast, the trunk–ground interactions dominate the total scattering as in Fig. 8(d).

Figs. 9 and 10 present the HH-polarized component scattering contributions from the trunk, crown, and ground layer at L- and X-bands, respectively. Both figures show that the aspen stand is trunk dominated since the ground–trunk scattering mechanism contributes most to the total scattering. Direct ground scattering decreases when the scattering angle θ increases. As for multiple frequencies, in the backscattering cases, the ground scattering

decreases when the frequency increases, but in the specular scattering cases, the figures show the opposite trend. Moreover, at L-band, scattering at small angles $\theta < 20°$, the ground scattering contribution is greater than the crown layer scattering in Fig. 9(a) and (b), while ground scattering is much lower than the crown scattering at X-band in Fig. 10(a) and (b). The crown layer scattering is much stronger at X-band than at L-band.

C. Scattering Angle Sensitivity to Canopy Parameters

The bistatic scattering's sensitivity to the canopy parameter changes is of great interest in optimizing radar system designs. In this section, we change various canopy parameters and analyze the results for L-band. We expect L-band to be particularly sensitive to the trunks, and hence to the biomass, which is one of the more commonly sought canopy parameters.

1) Aspen Stands: In this experiment, we simulate the microwave scattering in a specular direction cone surface ($\theta = \theta_0 = 45°$, $0 \leq \phi \leq 180°$) for four aspen stands with different trunk and branch diameters, which means the biomass of these four stands are different. While the other parameters are
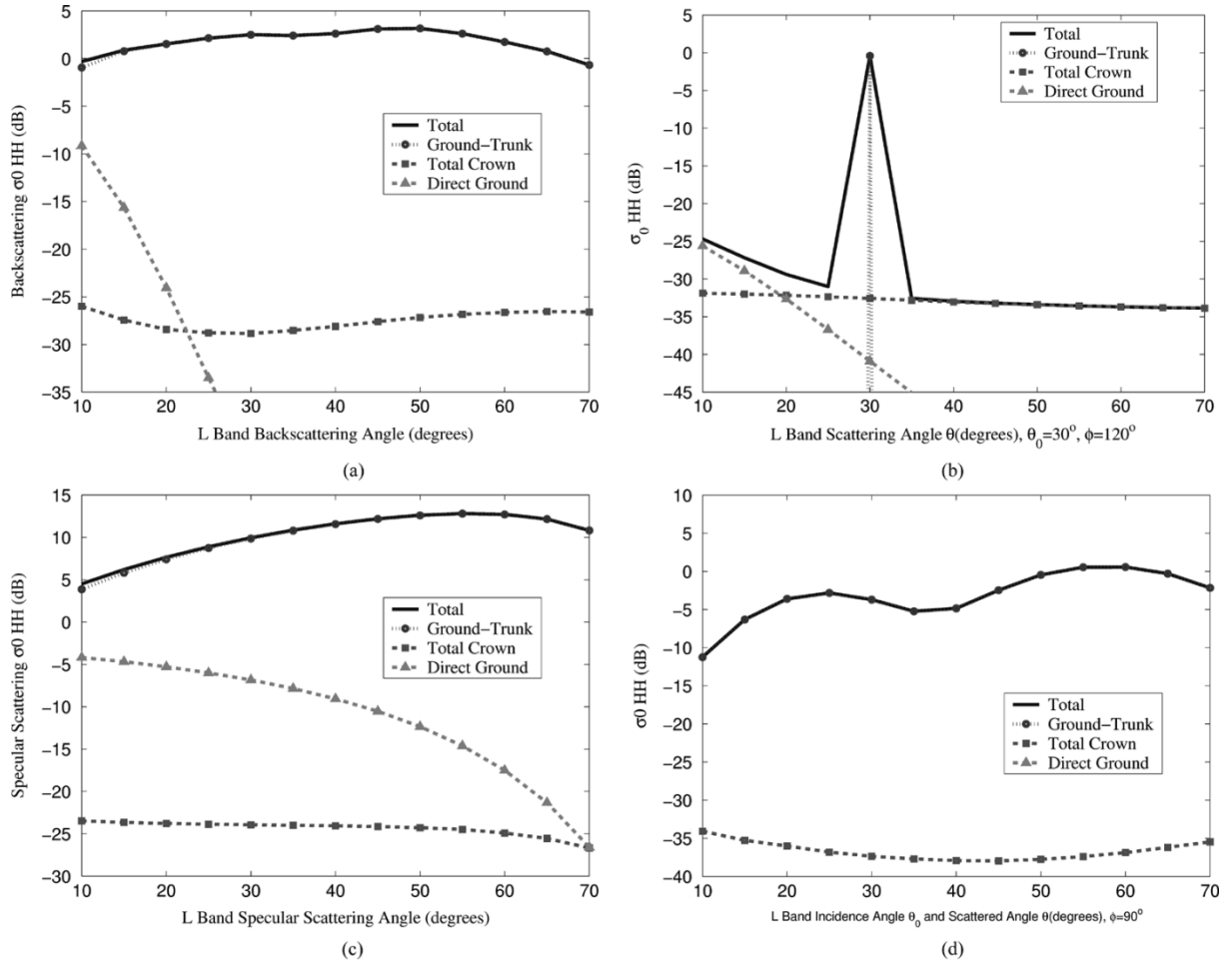
Fig. 9.   L-band HH-polarized canopy scattering component contributions versus scattering angle from aspen at (a) backscattering plane and (b) $\theta_0 = 30°$ and $\phi = 120°$. (c) Specular plane. (d) Perpendicular plane ($\theta = \theta_0, \phi = 90°$). The spike in (b) is due to specular scattering and is only wide in these plots due to the fact that we are sampling every $5°$ and connecting consecutive points with lines. (a) Backscattering. (b) Bistatic scattering. (c) Specular scattering. (d) Perpendicular plane.

the same as in Table I, Table III lists the aspen's trunk and branch diameters.

L-band HH-polarized bistatic simulation results for the four aspen stands are shown in Fig. 11. The direction $\phi = 0$ is the specular direction, and $\phi = 180°$ is for backscattering. In the backscattering and specular scattering directions, the changes of biomass cannot be captured by the simulated scattering coefficient σ_0. However, large differences among the four curves are observed at the ϕ range of $30°$ to $100°$. Most of the differences of σ_0 are contributed by trunk and ground interaction scattering. Fig. 11 also indicates that these are trunk-dominated canopies since the different branch sizes have little effect on the total scattering level, which is the reason that we cannot distinguish the two curves with the same trunk diameters but different branch diameters. Larger biomass density does not always generate high scattering coefficient as shown in Fig. 11, where the stands with small trunk diameters have larger σ_0 at angles of $30° \leq \phi < 70°$ and $100° \leq \phi \leq 120°$. However, there is not significant improvement to distinguish between the four stands using the VV-polarized bistatic measurement as demonstrated by

Fig. 12, where the difference between the four curves has a small dynamic range with respect to the angle.

2) White Spruce Stands: A similar approach is applied to four white spruce stands as in the last section. However, instead of changing the tree size parameters, we reduce the tree density from 2000 trees/ha to 1000 trees/ha, 666.7 trees/ha, and 500 trees/ha. Therefore, we have four stands of white spruce with the parameters listed in Table I except for the tree number density. This experiment is to simulate the forest density's effect on bistatic RCS. By decreasing the tree number density, we decrease the biomass density of the stands. The L-band HH-polarized simulation results in the specular direction cone surface are shown in Fig. 13. The largest dynamic range 21.3 dB occurs around $\phi = 30°$, which indicates that for these four stands of white spruce, the biomass differences can best be captured at $\phi = 30°$. The dynamic range for backscattering coefficients are 6.6 and 10.4 dB for specular scattering. The smallest dynamic range was 2.1 dB at $\phi = 90°$. Therefore, it would be inappropriate to place a receiver in the plane perpendicular to the incident direction for HH-polarized scattering coefficients if trying to measure biomass. The VH-polarized bistatic scat-
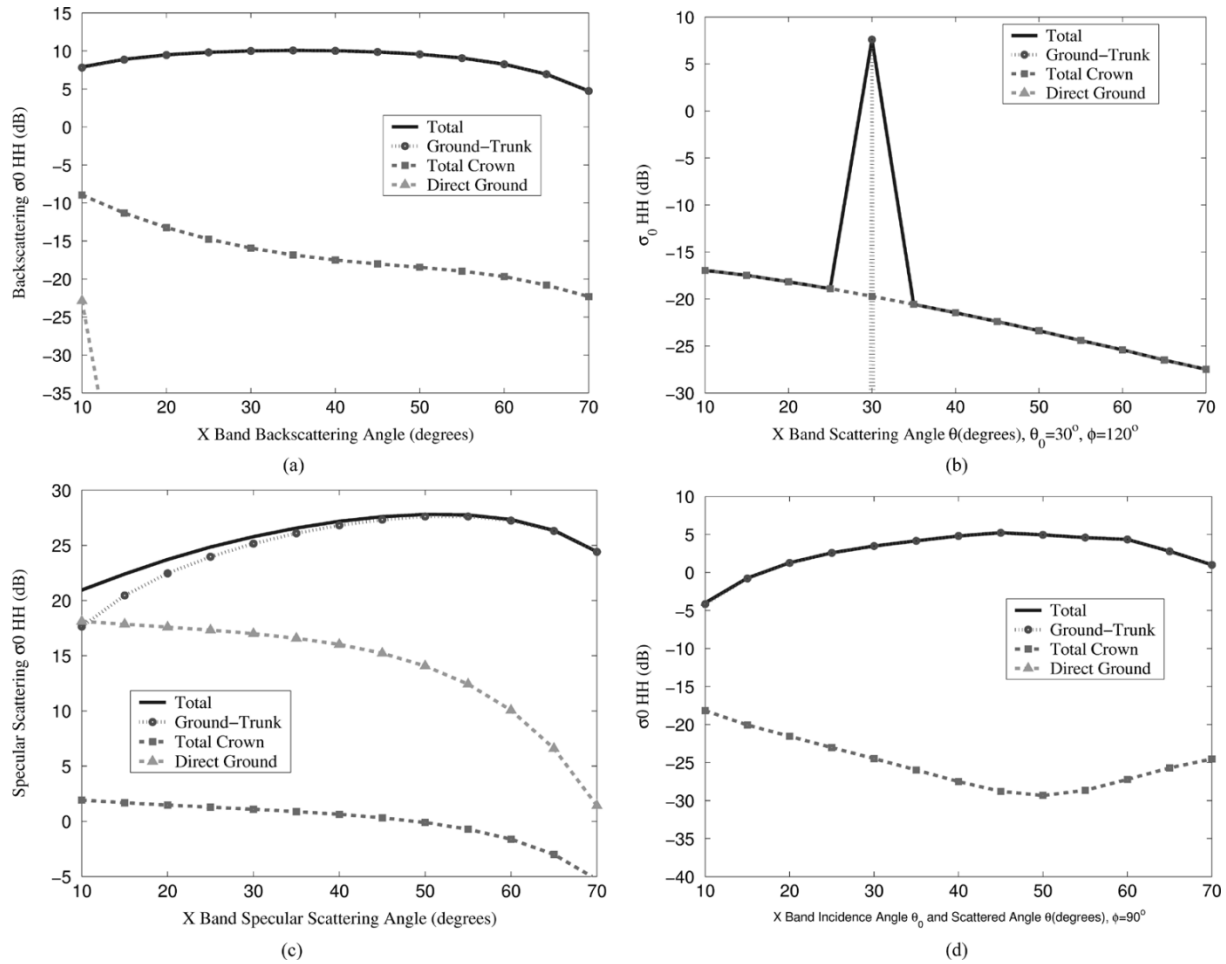
Fig. 10. X-band HH-polarized canopy scattering component contribution versus scattering angle from aspen at (a) backscattering plane and (b) $\theta_0 = 30°$ and $\phi = 120°$. (c) Specular plane. (d) Perpendicular plane ($\theta = \theta_0, \phi = 90°$). The spike in (b) is due to specular scattering and is only wide in these plots due to the fact that we are sampling every 5° and connecting consecutive points with lines. (a) Backscattering. (b) Bistatic scattering. (c) Specular scattering. (d) Perpendicular plane.

TABLE III
TRUNK AND BRANCH DIAMETERS FOR FOUR ASPEN STANDS

	Stand 1	Stand 2	Stand 3	Stand 4
Trunk Diameter	24cm	30cm	24cm	30cm
Branch Diameter	0.7cm	0.7cm	0.9cm	0.9cm

tering coefficient is also shown to be sensitive to the variation of tree density, as shown in Fig. 14.

In reference to these figures, it is noteworthy that the increased biomass density does not always cause higher microwave scattering. In Fig. 13, the stand with the highest tree density has the lowest scattering coefficient, while the stand with the lowest tree density has the strongest scattering coefficient. To explain this phenomenon, we need to probe into the complete scattering process of the forest canopy.

Less dense crown layers cause less attenuation from the upper level canopy; more energy can penetrate the crown layer; and so the trunk layer's contribution becomes more important. As a result, we expect more scattering from less dense canopy stands if large tree trunks are present. Moreover, with fewer trunks, the
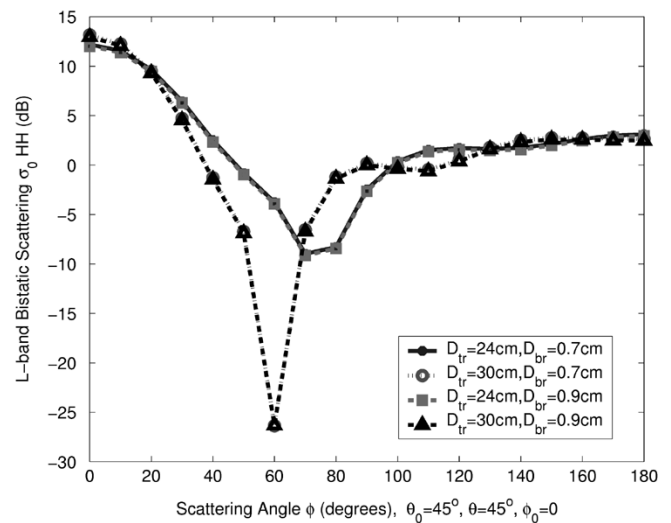

Fig. 11. L-band HH-polarized canopy scattering cross section versus scattering angle for four aspen stands. The variability in the responses is largely due to the change of the trunk diameter, showing very little sensitivity to the branch diameters. $\theta = \theta_0 = 45°$, and the azimuth angle ϕ is from 0° to 180°.

ground reflection of the crown scattering experiences less attenuation, as does the double-bounce crown scattering component.
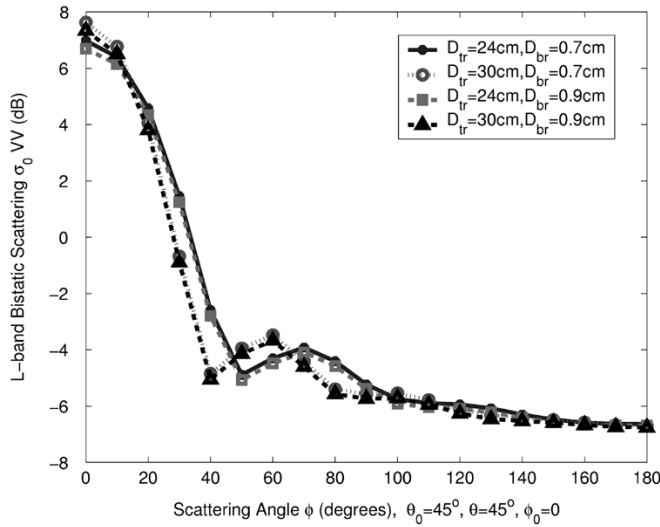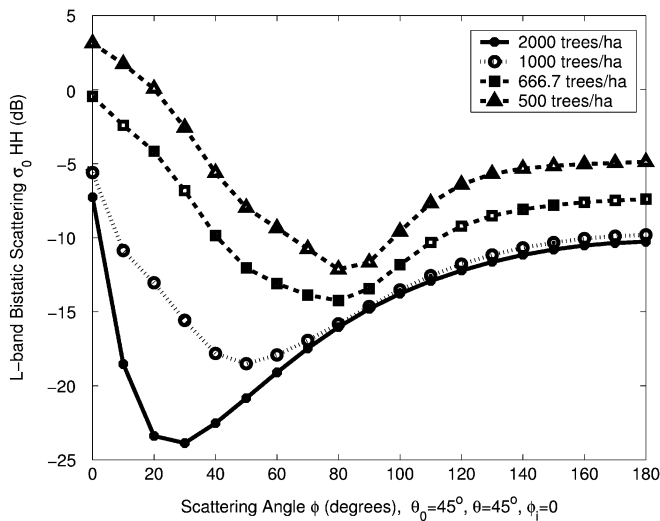
Fig. 12. L-band VV-polarized canopy scattering cross section versus scattering angle for four aspen stands. The variability in the responses is largely due to the change of the trunk diameter, showing very little sensitivity to the branch diameters. $\theta = \theta_0 = 45°$, and the azimuth angle ϕ is from 0° to 180°.

Fig. 14. L-band VH-polarized canopy scattering cross section versus scattering angle for four white spruce stands. $\theta = \theta_0 = 45°$, and the azimuth angle ϕ is from 0° to 180°.

Fig. 13. L-band HH-polarized canopy scattering cross section versus scattering angle for four white spruce stands. $\theta = \theta_0 = 45°$, and the azimuth angle ϕ is from 0° to 180°.

In addition, there is more ground scattering through the sparse canopies. All these factors together cancel the effect of the low tree density, hence increasing the total canopy scattering.

Fig. 15 shows the L-band HH-polarized canopy scattering component contributions to the total scattering for all stands in the specular direction cone surface. In Fig. 15(a), the large tree number density (2000 tree/ha) makes the stand a crown-dominated canopy, and the scattering from the trunk layer and ground are almost negligible. However, at half of this tree density (1000 tree/ha), the crown layer scattering relative contribution decreases, while the trunk layer scattering contribution increases, especially at small angles as shown in Fig. 15(b). When we further decrease the tree density (667 trees/ha), the trunk's contribution becomes more significant as shown in Fig. 15(c). Finally in Fig. 15(d), with only a quarter of the
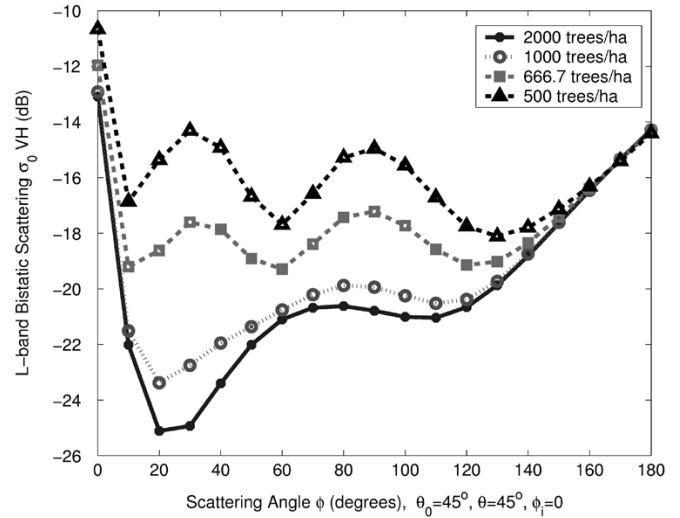
original tree density (500 trees/ha), the canopy becomes a trunk-dominated canopy, and the crown scattering becomes almost negligible. The ground surface scattering also rises as we decrease the canopy density; however, it is still very low compared to the trunk and crown layer scattering.

Not only do the canopies change from crown dominant to trunk dominant, the four components of crown scattering contributions also change. We plot the component contribution within the crown layer in Fig. 16. As can be seen from Fig. 16(a), direct scattering from the crown layer is the major contributor for the dense stand, while the double-bounce effect is too insignificant to be shown in the plot. In Fig. 16(b), the direct crown scattering is still dominant, but the crown–ground interaction scattering increases. In Fig. 16(c), the direct scattering and the crown–ground interaction are comparable for small ϕ angles. As in Fig. 16(d), the crown–ground scattering exceeds the direct crown scattering for small ϕ angles, and the double-bounce scattering is much higher. The ground–crown–ground double-bounce scattering is the weakest for all four cases.

D. Discussion

We have used the canopy stands used in the simple backscattering MIMICS [10] to validate our bistatic scattering model for the the special case of backscattering. Simulation results by the two models are shown to be consistent.

The bistatic RCS provides significantly more information about the mechanisms of canopy scattering and composition compared to the backscattered RCS. When $\theta = \theta_0$ is fixed and the azimuth angle ϕ is rotated around the target, the largest bistatic RCS is generally found at the specular receiving angles. For the trunk layer, HH-polarized trunk–ground interaction scattering is the strongest in the specular direction and weakest around the plane perpendicular to the incident direction. In contrast, VV-polarized trunk–ground scattering shows a slow
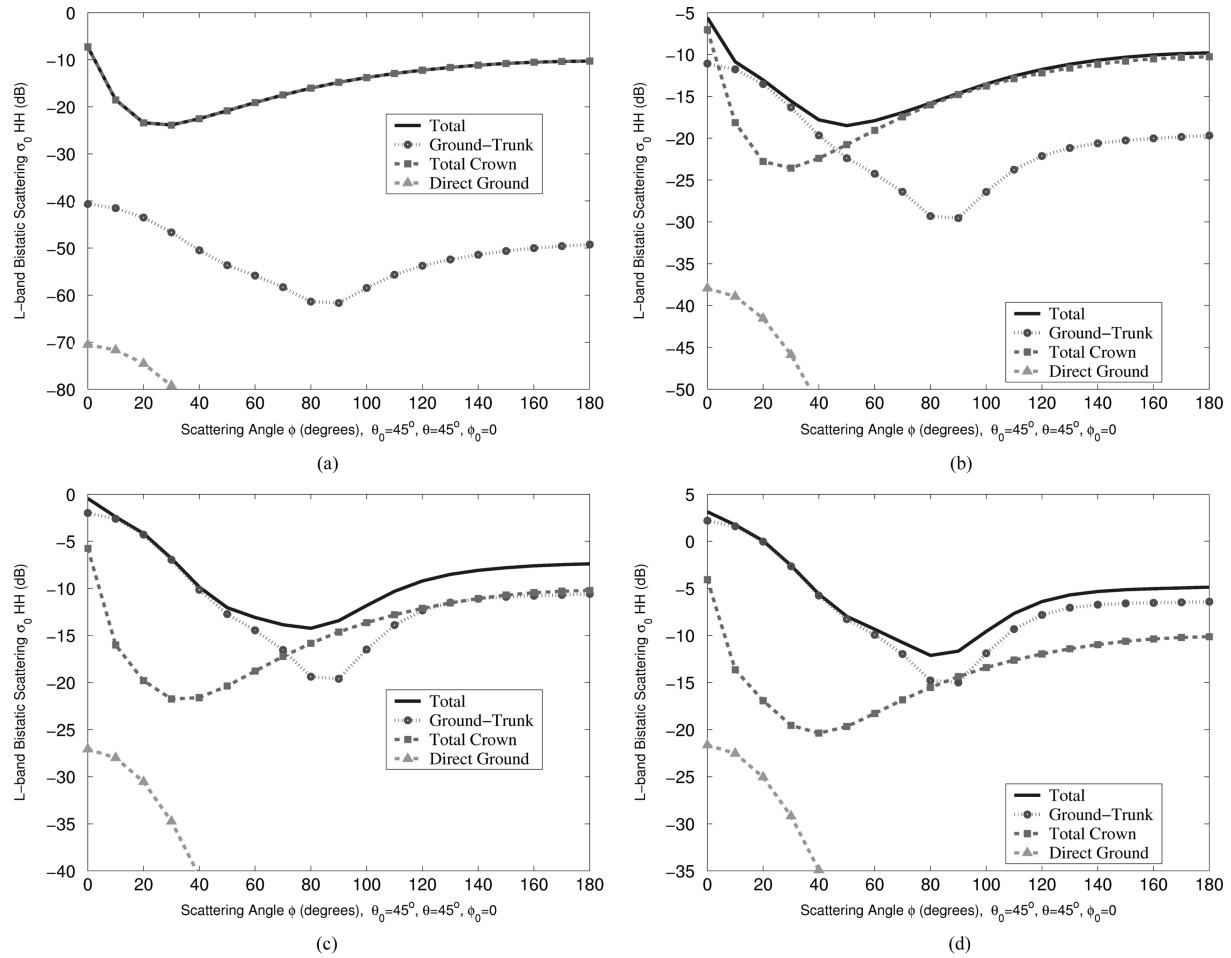
Fig. 15.   L-band HH-polarized canopy scattering component contributions versus scattering angle for four white spruce stands. $\theta = \theta_0 = 45°$, and the azimuth angle ϕ is from $0°$ to $180°$. Note that the ranges for the y axes are different for the different plots. (a) 2000 tree/ha. (b) 1000 trees/ha. (c) 666.7 trees/ha. (d) 500 trees/ha.

decreasing trend as the scattering angle ϕ changes from the specular direction to the backscattering direction.

Specular scattering from the rough ground surface is the greatest, whereas the direct backscattering from the ground is the lowest. The rough surface also causes more scattering at small elevation angles ($\theta < 20°$) and less scattering at large elevation angles ($\theta > 50°$). The effect of the ground on the total scattering cross section is larger at low frequencies where there is less attenuation by the crown and trunk layer.

Bi-MIMICS shows distinct sensitivities to the dimensions, density, angular distribution, and permittivity of the forest components and also to ground surface attributes. Changes of the parameters cause the canopy-dominant components to vary and the scattering compositions to change. Bistatic RCS offers more information than backscattering RCS due to the additional dimensions. Model simulations show that there are optimal angles for extracting canopy parameters that are superior to the backscattering angles, which are determined by the canopy composition and parameter distribution.

The simulation results presented in this paper represent a first-order RT-based model. The current first-order solution does

not include multiple-scattering mechanisms among scatterers; coherent effects, such as enhanced backscatter, are not therefore considered. However, multiple scattering among canopy elements is expected, particularly at high frequencies, where branch and foliage volume scattering dominates, and may cause an underestimation of the RCS at high frequencies.

At the moment, no actual bistatic SAR measurement data from vegetation are available to us for comparison with the model's simulation. Our future work includes conducting bistatic radar measurements on scaled forest models using our existing bistatic measurement facilities.

VI. CONCLUSION

Forest scattering modeling provides a tool to study the relationship between radar measurement and forest structures by simulating the scattering processing of microwave interaction with different components of the forest. In this paper, we present a bistatic microwave scattering model, which complements the existing backscattering MIMICS. It is based on radiative transfer theory and is designed to accommodate the bistatic
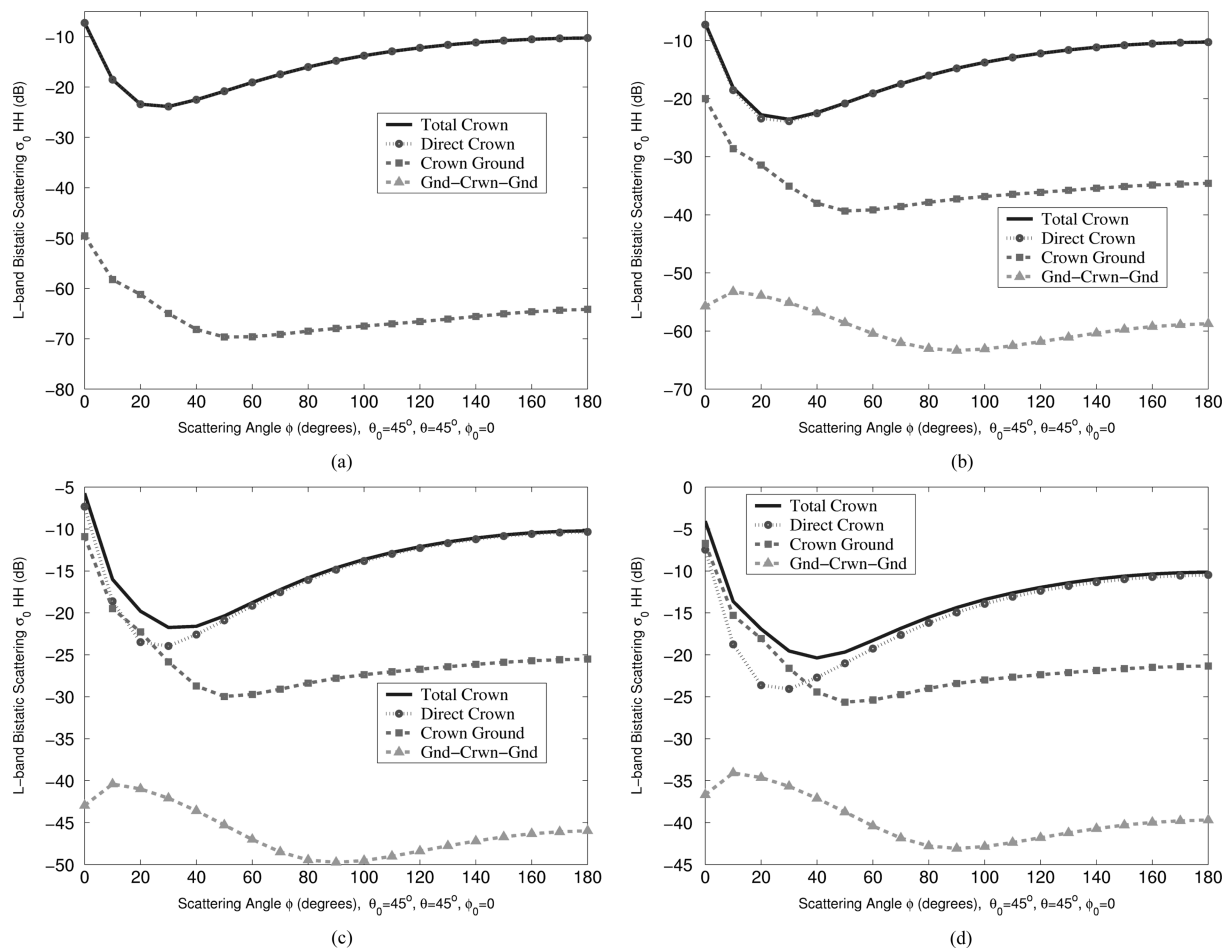
Fig. 16. L-band HH-polarized crown component scattering contributions versus scattering angle for four white spruce stands. $\theta = \theta_0 = 45°$, and the azimuth angle ϕ is from $0°$ to $180°$. Note that the ranges for the y axes are different for the different plots. (a) 2000 tree/ha. (b) 1000 trees/ha. (c) 666.7 trees/ha. (d) 500 trees/ha.

scattering simulation capability in anticipation of perspective bistatic radar systems.

Bi-MIMICS simulates SAR bistatic scattering for forest canopies characterized by input dimensional, geometrical, and dielectric parameters. As such, the model can be used to analyze the relationship between canopy parameters and the scattering coefficient, especially with the advantage of multiple observation angles. From the model, differences in tree height, moisture content, and biomass can be simulated by simply changing the model inputs and by analyzing the contribution of each individual layer to the bistatic RCS.

Bi-MIMICS is parameterized to selected tree canopies with different canopy structures and density. A number of bistatic RCS values are simulated at various bistatic angles. The simulation results demonstrate the bistatic scattering mechanisms and the potential application of bistatic measurement. Scattering behavior of canopy components are varied with respect to the bistatic geometry to show their respective sensitivities.

The radar response at multiple measurement angles, in addition to multiple frequencies and polarizations, can be used to study the potential retrieval of forest biomass and other vegetation parameters, which is the goal of our ongoing work. Our

future work also includes performing laboratory bistatic measurement for model validation and extending the current solution to higher orders.

REFERENCES

[1] D. J. McLaughlin, Y. Wu, W. G. Stevens, X. Zhang, M. J. Sowa, and B. Weijers, "Fully polarimetric bistatic radar scattering behavior of forested hills," *IEEE Trans. Antennas Propagat.*, vol. 50, no. 2, pp. 101–100, Feb. 2002.

[2] M. Soumekh, "Bistatic synthetic aperture radar inversion with application in dynamic object imaging," *IEEE Trans. Signal Process.*, vol. 39, no. 9, pp. 2044–2055, Sep. 1991.

[3] F. T. Ulaby, T. E. V. Deventer, J. R. East, T. F. Haddock, and M. E. Coluzzi, "Bistatic scattering characterization of complex objects," *IEEE Trans. Geosci. Remote Sens.*, vol. 26, no. 3, pp. 229–243, May 1988.

[4] J. Robert, L. Eigel, P. J. Collins, J. Andrew, J. Terzuoli, G. Nesti, and J. Fortuny, "Bistatic scattering characterization of complex objects," *IEEE Trans. Geosci. Remote Sens.*, vol. 38, no. 5, pp. 2078–2092, Sep. 2000.

[5] K. Sarabandi and A. Nashashibi, "A novel bistatic scattering matrix measurement technique using a monostatic radar," *IEEE Trans. Antennas Propagat.*, vol. 44, no. 1, pp. 41–50, Jan. 1996.

[6] R. J. Burkholder, L. J. Gupta, and J. T. Johnson, "Comparison of monostatic and bistatic radar images," *IEEE Antennas Propagat. Mag.*, vol. 45, no. 3, pp. 41–50, Jun. 2003.

[7] D. Zahn and K. Sarabandi, "Simulation of bistatic scattering for assessing the application of existing communication satellites to remote sensing of rough surfaces," in *Proc. IGARSS*, vol. 4, Jul. 2000, pp. 1528–1530.

[8] H. D. Griffiths, C. J. Baker, J. Baubert, N. Kitchen, and M. Treagust, "Bistatic radar using satellite-borne illuminators," *Radar*, pp. 1–5, Oct. 2002.

[9] R. H. Lang and J. S. Sidhu, "Electromagnetic backscattering from a layer of vegetation: A discrete approach," *IEEE Trans. Geosci. Remote Sens.*, vol. 21, no. 1, pp. 177–186, Jan. 1993.

[10] F. T. Ulaby, K. Sarabandi, K. McDonald, M. Whitt, and M. C. Dobson, "Michigan Microwave Canopy Scattering model (MIMICS)," Univ. Michigan, Ann Arbor, Tech. Rep. 022486-T-1, Jul. 1988.

[11] S. L. Durden, J. J. V. Zyl, and H. A. Zebker, "Modeling and observation of the radar polarization signature of forested areas," *IEEE Trans. Geosci. Remote Sens.*, vol. 27, no. 3, pp. 290–301, May 1989.

[12] J. A. Richards, G. Q. Sun, and D. S. Simonett, "L-band radar backscattering modeling of forest stands," *IEEE Trans. Geosci. Remote Sens.*, vol. 25, no. 4, pp. 487–498, Jul. 1987.

[13] Y.-C. Lin and K. Sarabandi, "Electromagnetic scattering model for a tree trunk above a tilted ground plane," *IEEE Trans. Geosci. Remote Sens.*, vol. 33, no. 4, pp. 1063–1070, Jul. 1995.

[14] G. Picard, T. L. Toan, S. Quegan, Y. Caraglio, and T. Castel, "Radiative transfer modeling of cross-polarized backscatter from a pine forest using the discrete ordinate and eigenvalue method," *IEEE Trans. Geosci. Remote Sens.*, vol. 42, no. 8, pp. 1720–1730, Aug. 2004.

[15] P. Liang, M. Moghaddam, L. E. Pierce, and R. M. Lucas, "Radar backscattering model for multilayer mixed-species forests," *IEEE Trans. Geosci. Remote Sens.*, vol. 43, no. 11, pp. 2612–2626, Nov. 2005.

[16] K. Sarabandi and Y.-C. Lin, "Simulation of interferometric sar response for characterizing the scattering phase center statistics of fores canopies," *IEEE Trans. Geosci. Remote Sens.*, vol. 38, no. 1, pp. 115–125, Jan. 2000.

[17] S. S. Saatchi and K. C. McDonald, "Coherent effects in microwave backscattering models for forest canopies," *IEEE Trans. Geosci. Remote Sens.*, vol. 35, no. 4, pp. 1032–1044, Jul. 1997.

[18] F. T. Ulaby, R. K. Moore, and A. K. Fung, *Microwave Remote Sensing: Active and Passive*. Dedham, MA: Artech House, 1986, vol. III, Volume Scattering and Emission Theory, Advanced System and Applications.

[19] K. C. McDonald, M. C. Dobson, and F. T. Ulaby, "Using MIMICS to model L-band multiangle and multitemporal backscatter from a walnut orchard," *IEEE Trans. Geosci. Remote Sens.*, vol. 28, no. 4, pp. 477–491, Jul. 1990.

[20] ——, "Modeling multifrequency diurnal backscatter from a walnut orchard," *IEEE Trans. Geosci. Remote Sens.*, vol. 29, no. 6, pp. 852–863, Nov. 1991.

[21] M. C. Dobson, K. McDonald, and F. T. Ulaby, "Modeling of forest canopies and analyses of polarimetric SAR data," Univ. Michigan, Ann Arbor, Tech. Rep. 026143-1-F, 1989.

[22] F. T. Ulaby and C. ELachi, Eds., *Radar Polarimetry for Geoscience Applications*. Dedham, MA: Artech House, 1990.

[23] K. C. McDonald, "Modeling microwave backscatter from tree canopies," Ph.D. dissertation, Univ. Michigan, Ann Arbor, 1991.

[24] F. T. Ulaby and M. El-Rayes, "Microwave dielectric spectrum of vegetation, part II: Dual-dispersion model," *IEEE Trans. Geosci. Remote Sens,*, vol. GE-25, pp. 550–557, 1987.

[25] M. T. Hallikainen, F. T. Ulaby, M. C. Dobson, M. El-Rayes, and L.-K. Wu, "Microwave dielectric behavior of wet soil—Part I: Empirical models and experimental observations," *IEEE Trans. Geosci. Remote Sens.*, vol. GE-23, no. 1, pp. 23–34, Jan. 1985.

[26] R. De Roo, "Theory and measurement of bistatic scattering of X-band microwaves from rough dielectric surfaces," Ph.D. dissertation, Univ. Michigan, Ann Arbor, 1996.
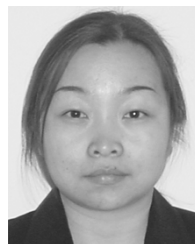
Pan Liang (S'02) received the B.S. degree in electrical engineering from Xidian University, Xi'an, China, the M.S. degree in spacecraft design from the Center for Space Science and Applied Research, Chinese Academy of Sciences, Beijing, China, and the Ph.D. degree in electrical engineering from The University of Michigan, Ann Arbor, in 1995, 1998, and 2004, respectively.

She is currently a Research Associate at Atmospheric and Environmental Research, Inc., Lexington, MA, where she has been working in the microwave remote sensing group.

Leland E. Pierce (S'85–M'89–SM'01) received the B.S. degrees in both electrical and aerospace engineering in 1983, and the M.S. and Ph.D. degrees in electrical engineering in 1986 and 1991, respectively, all from The University of Michigan, Ann Arbor.

Since 1991, he has been the Head of the Microwave Image Processing Facility within the Radiation Laboratory, Electrical Engineering and Computer Science Department, The University of Michigan, where he is responsible for research into the uses of polarimetric SAR systems for remote sensing applications, specifically forest canopy parameter inversion.

Mahta Moghaddam (S'86–M'87–SM'02) received the B.S. degree in 1986 from the University of Kansas, Lawrence (with highest distinction) and the M.S. and Ph.D. degrees in 1989 and 1991, respectively, from the University of Illinois, Urbana-Champaign, all in electrical and computer engineering.

She is currently an Associate Professor of electrical engineering and computer science and a member of the Radiation Laboratory at the University of Michigan, Ann Arbor, where she has been since 2003. From 1991 to 2003, she was with the Radar Science and Engineering Section, Jet Propulsion Laboratory (JPL), California Institute of Technology, Pasadena. At JPL, she introduced innovative approaches and algorithms for quantitative interpretation of multichannel SAR imagery based on analytical inverse scattering techniques applied to complex and random media. She also introduced a quantitative approach for data fusion by combining SAR and optical remote sensing data for nonlinear estimation of vegetation and surface parameters. Her other contributions include the development of new radar instrument and measurement technologies for subsurface and subcanopy characterization. She is and has been Principal and Co-Investigator on several research projects and has authored or coauthored over 100 journal and conference papers. Her other responsibilities have included being a Systems Engineer for the Cassini Radar and the JPL Science group Lead for the LightSAR project, and she has served on the Science Chair of the JPL Team X (Advanced Mission Studies Team). She is has led a NASA Instrument Incubator Program project to develop advanced technologies and measurement concepts for a low-frequency (UHF and VHF) spaceborne SAR instrument for global measurement of deep and subcanopy soil moisture.

Dr. Moghaddam has been Chair and Co-Chair of several conference sessions and Co-Chair of the NASA/ESTO Workshop Radar panel for defining future radar technologies and measurement scenarios. She is a member of URSI Commission B, the Electromagnetics Academy, Phi Kappa Phi, Tau Beta Pi, and Eta Kappa Nu.